Petroleum Science 22 (2025) 1946–1958

Contents lists available at ScienceDirect

Petroleum Science

journal homepage: www.keaipublishing.com/en/journals/petroleum-science

Original Paper

A novel logging method for detecting highly resistive formations in oil-based mud using high-frequency electrodes

Kang-Kang Wu [a, b], Lei Wang [a, b, *], Shao-Gui Deng [a, b], Xue-Wen Kou [a, b]

[a] State Key Laboratory of Deep Oil and Gas, China University of Petroleum (East China), Qingdao, 266580, Shandong, China
[b] School of Geosciences, China University of Petroleum (East China), Qingdao, 266580, Shandong, China

A R T I C L E I N F O

Article history:
Received 30 September 2024
Received in revised form
27 December 2024
Accepted 10 March 2025
Available online 12 March 2025

Edited by Meng-Jiao Zhou

Keywords:
Oil-based mud
Highly-resistive
High-frequency electrode
Bulking electrode
Depth of investigation

A B S T R A C T

The oil-based mud (OBM) borehole measurement environment presents significant limitations on the application of existing electrical logging instruments in high-resistance formations. In this paper, we propose a novel logging method for detection of high-resistance formations in OBM using high-frequency electrodes. The method addresses the issue of shallow depth of investigation (DOI) in existing electrical logging instruments, while simultaneously ensuring the vertical resolution. Based on the principle of current continuity, the total impedance of the loop is obtained by equating the measurement loop to the series form of a capacitively coupled circuit. and its validity is verified in a homogeneous formation model and a radial two-layer formation model with a mud standoff. Then, the instrument operating frequency and electrode system parameters were preferentially determined by numerical simulation, and the effect of mud gap on impedance measurement was investigated. Subsequently, the DOI of the instrument was investigated utilizing the pseudo-geometric factor defined by the real part of impedance. It was determined that the detection depth of the instrument is 8.74 cm, while the effective vertical resolution was not less than 2 cm. Finally, a focused high-frequency electrode-type instrument was designed by introducing a pair of focused electrodes, which effectively enhanced the DOI of the instrument and was successfully deployed in the Oklahoma formation model. The simulation results demonstrate that the novel method can achieve a detection depth of 17.40 cm in highly-resistive formations drilling with OBM, which is approximately twice the depth of detection of the existing oil-based mud microimager instruments. Furthermore, its effective vertical resolution remains at or above 2 cm, which is comparable to the resolution of the existing OBM electrical logging instrument.

1. Introduction

The global oil and gas industry are currently undergoing a significant transformation, characterized by the emergence of new technologies and a shift towards unconventional sources of energy (Aguilera and Radetzki, 2014; Davis, 2018). The development of deep oil and gas and shale oil and gas represents a crucial phase in the evolution of the industry, offering new avenues for strategic resource utilization (Zou et al., 2020). The use of OBM in high-temperature deep wells, directional slanting and horizontal wells are commonplace due to the advantages they offer in terms of reducing oil and gas formation damage, improving drilling speed and increasing borehole stability (Morton et al., 2005; Færgestad and Strachan, 2014; Hindry, 1941). As a result, the technology has become an important tool for shale oil and gas and deep oil and gas exploration and development. The OBM environment presents novel challenges to the existing electrical logging technology. Firstly, OBM is electrically insulating, which obstructs the current pathway and renders the direct current (DC) resistivity logging, exemplified by lateral logging, inapplicable. Secondly, it is frequently the case that shale oil and gas and deep oil and gas reservoirs exhibit resistivities within the range of a few hundreds or even a few thousands ohm meter, which exceeds the scope of the current induction logging, and brings a lot of uncertainty to the practical application (Hong and Yang, 2011; Hou et al., 2013; Li et al., 2015; Wang et al., 2019; Jiang et al., 2021). It is therefore of great practical significance to study a new logging method applicable to the measurement of highly-resistive formations in OBM.

---

* Corresponding author.
E-mail address: leiwang1989@upc.edu.cn (L. Wang).

https://doi.org/10.1016/j.petsci.2025.03.010

Due to the high resistivity of OBM, it will isolate the conduction current, which makes the traditional water-based mud electrical imaging logging instruments no longer applicable. In order to address the issue of challenging environmental detection of oil-based mud measurements, a synthesis of the prevailing solutions are presented as follows: (1) Enhance the conductivity of oil-based mud through additives and use low-frequency measurement methods (Thaemlitz, 2004; Zanten, 2014). (2) Scrape off the high mud cake by mechanical means to form a direct current path (Christie and Schoch, 2007; Gao et al., 2017, 2019). (3) Four-terminal measurement method (Cheung et al., 2001). (4) Capacitive coupling method. These techniques facilitate the formation of a current path between the electrode and the formation. The design of oil-based mud logging instruments, such as the Oil-Based Mud Micro-imager (OBMI) and Earth Imager (EI), is based on the principle of capacitive coupling (Bloemenkamp et al., 2014; Bespalov and Itskovich, 2008). These instruments represent a new generation of electrical imaging logging tools that are suitable for use in non-conductive mud openhole wells. The aforementioned instruments employ high-frequency currents to traverse the oil-based mud and into the formation. Through the utilization of a high-resolution array microelectrode scanning technique, the geological characteristics of the wellbore formation are displayed in an intuitive and clear manner. However, the method is significantly influenced by the high-resistance measurement environment, resulting in a limited detection depth. Furthermore, the imaging process only captures resistivity information in the vicinity of the borehole wall, preventing the effective acquisition of formation information from distant locations. This inherent limitation hinders the practical engineering applications of the method.

In order to solve the problem of difficult resistivity detection for high-resistance formations in OBM with shallow detection depth, the author designed an focusing electrode-type pad structure based on the principle of capacitive coupling, and examined the complex effects of the transmitting frequency of the instrument, and the sizes and positions of the electrodes on the logging response in different formation models, and analyzed the influence of each parameter on the detection of the resistivity of the formation. By selecting the preferred operating frequency and optimizing the electrode size, effective measurement of high-resistance formation resistivity in oil-based mud is achieved. Compared with the existing OBM electrical imaging technology, the radial detection performance of the instrument is effectively improved while ensuring the vertical resolution of the formation, which provides a possibility and a method for the detection of resistivity in highly-resistive formations drilling with OBM.

2. Physics of resistivity measurement with high-frequency electrodes

2.1. Principle of high frequency-electrodes measurement

As illustrated in Fig. 1, the measurement electrode pad features a single transmitting electrode paired with two symmetrical return electrodes, each insulated from the others. The symmetric return electrodes have been designed in order to minimize the effects of the instrument as it passes through the layer interface (Bloemenkamp et al., 2014). Due to the capacitive properties of oil-based drilling mud, current continuity between the electrode and formation can be achieved by applying a high-frequency alternating current (AC) voltage of a specific amplitude, enabling current to flow through the oil-based mud into the formation (Habashy et al., 2017; Gao et al., 2024). In this study, a voltage of 1 V is applied to the transmitting electrode, allowing the current generated to penetrate the formation after passing through the mud standoff and then return to the return electrode via the standoff. According to Ohm's law, the loop impedance Z can be calculated by measuring the loop current I and the voltage U (Growcock et al., 1994; San et al., 2008). Additionally, the apparent resistivity (R_a) can be determined using the instrument constant K, which is obtained through experimental calibration or by means of numerical simulation via the finite element method (Ke, 2008; Wang et al., 2017).

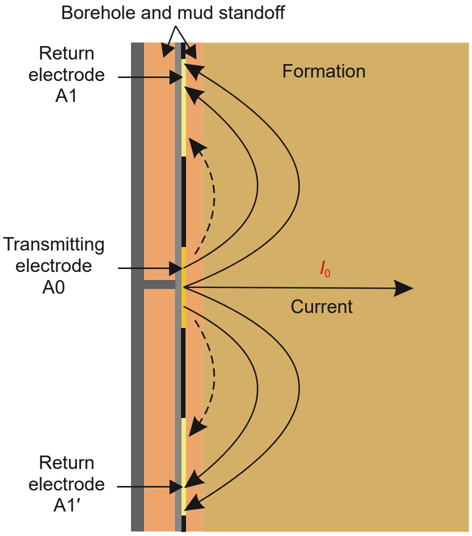

Fig. 1. Working principle of resistivity logging in OBM.

$$R_a = K \cdot Z = \frac{KU}{I} \tag{1}$$

The current flow circuit is simplified to the path shown in Fig. 2. When the voltage U is applied between A0 and A1, the current I_0 generated sequentially passes through the mud standoff (thickness = H_1) between A0 and the formation, the undisturbed formation (thickness = H_2), and the mud standoff (thickness = H_1) between the formation and A1, thereby establishing the current pathway. The electric field strengths in each region are represented as E_1, E_2, and E_3. Based on the continuity theorem of current, we can derive:

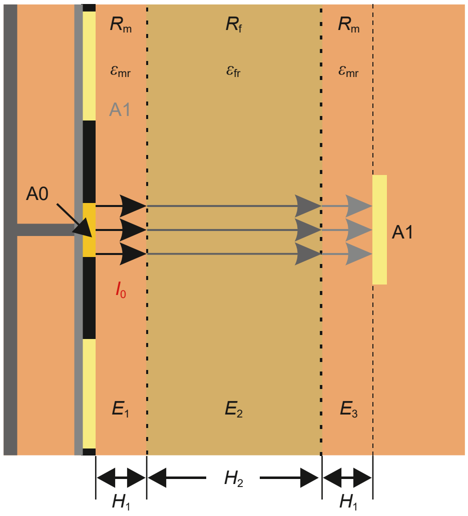

Fig. 2. Equivalent current loop for interpreting.

$$I_0=\widehat{\sigma}_1\cdot E_1\cdot S_1=\widehat{\sigma}_2\cdot E_2\cdot S_1=\widehat{\sigma}_3\cdot E_3\cdot S_2 \tag{2}$$

where $\widehat{\sigma}_1=\widehat{\sigma}_3=1/R_\mathrm{m}+j\omega\varepsilon_\mathrm{m}$, is the complex conductivity of the mud and $\widehat{\sigma}_2=1/R_\mathrm{f}+j\omega\varepsilon_\mathrm{f}$, is the complex conductivity of the formation. R_m, ε_m, R_f and ε_f refer to the resistivity and permittivity of mud standoff and formation, respectively. ω is angular frequency, S_1 is the area of the transmitting electrode, and S_2 is the area of the return electrode. $j=\sqrt{-1}$ is an imaginary unit.

According to the relationship between voltage and electric field intensity, it can be obtained:

$$U=E_1\cdot H_1+E_2\cdot H_2+E_3\cdot H_1 \tag{3}$$

Substitute Eq. (2) into the above formula, and define the total impedance Z of the loop, then

$$Z=\frac{U}{I_0}=\frac{1}{S_1}\cdot\frac{H_1}{\frac{1}{R_\mathrm{m}}+j\omega\varepsilon_\mathrm{m}}+\frac{1}{S_1}\cdot\frac{H_2}{\frac{1}{R_\mathrm{f}}+j\omega\varepsilon_\mathrm{f}}+\frac{1}{S_2}\cdot\frac{H_1}{\frac{1}{R_\mathrm{m}}+j\omega\varepsilon_\mathrm{m}} \tag{4}$$

Further, the loop impedance is written as the sum of the real and imaginary parts:

$$\begin{aligned}Z=&\left[\frac{(c+1)\cdot H_1}{S_1}\cdot\frac{R_\mathrm{m}}{1+(\omega\varepsilon_\mathrm{m}R_\mathrm{m})^2}+\frac{H_2}{S_1}\cdot\frac{R_\mathrm{f}}{1+\left(\omega\varepsilon_\mathrm{f}R_\mathrm{f}\right)^2}\right]\\&+j\cdot\left[\frac{(c+1)\cdot H_1}{S_1}\cdot\frac{\omega\varepsilon_\mathrm{m}R_\mathrm{m}^2}{1+(\omega\varepsilon_\mathrm{m}R_\mathrm{m})^2}+\frac{H_2}{S_1}\cdot\frac{\omega\varepsilon_\mathrm{f}R_\mathrm{f}^2}{1+\left(\omega\varepsilon_\mathrm{f}R_\mathrm{f}\right)^2}\right]\end{aligned} \tag{5}$$

where c is the ratio of the area of the transmitting electrode to the area of the return electrode, and equals to the ratio of their lengths.

Eq. (4) can be interpreted as a series of three impedances (Guner et al., 2021). The three components on the right represent the mud standoff impedance Z_m between the transmitting electrode and the formation, the formation impedance Z_f, and the mud standoff impedance $Z_\mathrm{m}{'}$ between the return electrode and the formation, respectively.

2.2. Capacitance-coupled equivalent circuit

Based on the above derivation, each part of the impedance can be considered as a parallel coupling of capacitor C and resistor r (Bespalov and Itskovich, 2008; Guner et al., 2021). Taking the formation impedance Z_f as an example, the coupling principle is shown in Fig. 3(a). Fig. 3(b) depicts the equivalent circuit of the loop. For traditional water-based mud and oil-based mud resistivity imaging instruments, due to the transmitting electrode being a button electrode with a diameter of a few millimeters, its impedance is much greater than the impedance of the return electrode, typically leading to the neglect of the return electrode impedance (Chen, 2001). In this study, the effects of the size and arrangement positions of both the transmitting and return electrodes on the detection of formation resistivity are considered simultaneously. Therefore, each part of the impedance in the circuit cannot be ignored.

From the capacitive coupling model in Fig. 3(a), the equivalent resistor r_f and equivalent capacitor C_f of the formation can be expressed as

$$\begin{aligned}r_\mathrm{f}&=R_\mathrm{f}\cdot\frac{H_2}{S_1}\\C_\mathrm{f}&=\frac{\varepsilon_\mathrm{fr}\cdot\varepsilon_0\cdot S_1}{H_2}\end{aligned} \tag{6}$$

Then, the formation impedance Z_f can be written as

$$\begin{aligned}Z_\mathrm{f}&=\frac{1}{\frac{1}{r_\mathrm{f}}+j\omega C_\mathrm{f}}=\frac{H_2}{S_1}\cdot\frac{1}{\frac{1}{R_\mathrm{f}}+j\omega\varepsilon_\mathrm{fr}\varepsilon_0}\\&=\frac{H_2}{S_1}\cdot\left[\frac{R_\mathrm{f}}{1+\left(\omega\varepsilon_\mathrm{f}R_\mathrm{f}\right)^2}-j\frac{\omega\varepsilon_\mathrm{f}R_\mathrm{f}^2}{1+\left(\omega\varepsilon_\mathrm{f}R_\mathrm{f}\right)^2}\right]\end{aligned} \tag{7}$$

where ε_fr is the relative permittivity of the formation.

For the homogeneous formation model, the depth of current into the formation is assumed to be $H_2{'}$, so that $H_2{'}=H_2+\Delta H$. Then, according to Eq. (5) and Eq. (7), the impedance difference ΔZ between the homogeneous formation and the formation model with a mud layer can be calculated.

$$\begin{aligned}\Delta Z&=\Delta\Re(Z)+j\cdot\Delta\Im(Z)\\&=\left[\frac{\Delta H}{S_1}\cdot\frac{R_\mathrm{f}}{1+\left(\omega\varepsilon_\mathrm{f}R_\mathrm{f}\right)^2}-\frac{(c+1)\cdot H_1}{S_1}\cdot\frac{R_\mathrm{m}}{1+(\omega\varepsilon_\mathrm{m}R_\mathrm{m})^2}\right]\\&+j\cdot\left[\frac{(c+1)\cdot H_1}{S_1}\cdot\frac{\omega\varepsilon_\mathrm{m}R_\mathrm{m}^2}{1+(\omega\varepsilon_\mathrm{m}R_\mathrm{m})^2}-\frac{\Delta H}{S_1}\cdot\frac{\omega\varepsilon_\mathrm{f}R_\mathrm{f}^2}{1+\left(\omega\varepsilon_\mathrm{f}R_\mathrm{f}\right)^2}\right]\end{aligned} \tag{8}$$

An AC voltage source is applied to the transmitting electrode, and the measured loop current is a complex current. Assuming that the thickness of the mud standoff is 0, i.e., a homogeneous formation model, the real part $\Re(I_0)$ and imaginary part $\Im((I_0)$ of the loop current in the homogeneous formation model can be obtained from Eq. (4).

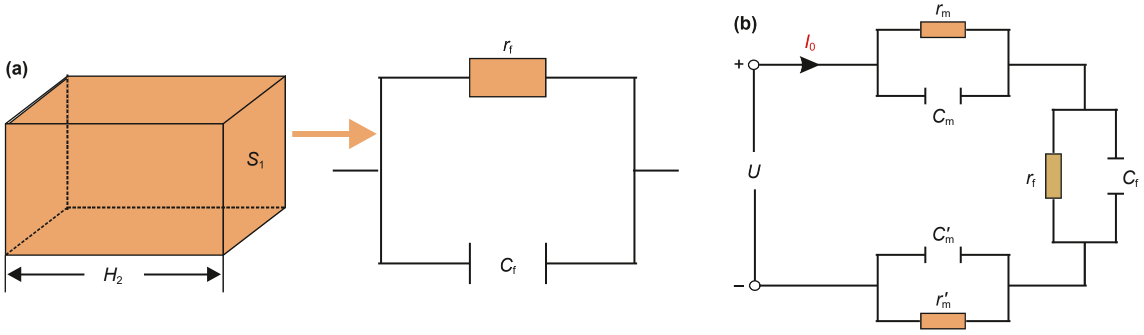

Fig. 3. Principle of capacitive coupling and equivalent circuit: **(a)** Capacitive coupling model; **(b)** equivalent circuit.

$$\begin{aligned}\Re(I_0) &= \frac{S_1}{H_2}\cdot\frac{U}{R_\mathrm{f}}\\ \Im(I_0) &= \frac{S_1}{H_2}\cdot U\omega\varepsilon_\mathrm{f}\end{aligned} \tag{9}$$

Furthermore, the ratio of imaginary part to real part of current $\Im((I_0)/\Re(I_0)$ is obtained, which is also equal to the ratio of imaginary part to real part of impedance in value.

$$\Im(I_0)\Big/\Re(I_0) = \omega\varepsilon_\mathrm{f}R_\mathrm{f} \tag{10}$$

2.3. Verification of work principle

Based on the above derivation and integration of numerical simulations, the responses of the current and impedance signals within a homogeneous formation model are investigated. The borehole radius was 0.1016 m (4 inch). Considering the calculation speed and accuracy, the formation model was set to a radius of 2.0 m, the formation thickness was 4.0 m, and the instrument was located at the midpoint of the formation. The lengths of both the transmitting and symmetrical return electrodes are set to 10 cm, with an electrode spacing L also being 10 cm (where L is the distance between the adjacent ends of the emitting electrode A0 and the return electrode A1/A1′). The range of formation resistivity spans from 0.1 to 10000 $\Omega\cdot$m, while considering a relative dielectric constant of 15 for the formation. An AC voltage of 1 V is applied to the transmitting electrode at frequencies ranging from 0.1 to 20 MHz. The current and impedance signals at the emitting electrode are then calculated accordingly.

Two sets of curves are included in each of the plots shown in Fig. 4(a)–(e), using a double logarithmic coordinate system. The solid lines represent the real part, imaginary part, and the ratio of the imaginary part to the real part of the current (impedance) obtained through numerical simulation. Conversely, the dashed lines depict results derived from calculations using an equivalent circuit model. (1) The two sets of curves overlap exactly, demonstrating the validity of the equivalent circuit model. (2) Combined with Eq. (9) and Fig. 4(a) and (b), the real part of the current is anticorrelated with R_f and is not affected by frequency. The imaginary part of the current is insensitive to R_f and is related to the magnitude of ε_f. (3) In the low-resistivity region ($R_\mathrm{f} < 20\ \Omega\cdot\mathrm{m}$), the real part of the impedance curves coincide at different frequencies and are linearly correlated with the R_f. Beyond this range, the impedance signal at 20 MHz begins to decrease as R_f increases, and then the other curves show the same pattern, and the reversal point of the curve is related to the magnitude of $\omega\cdot\varepsilon_\mathrm{f}\cdot R_\mathrm{f}$ (Fig. 4(c)), which is called "dielectric rollover" (Bespalov and Itskovich, 2008; Guner et al., 2021; Gao et al., 2024). (4) In the high-frequency and high-resistivity region, the imaginary part of the impedance is less sensitive to R_f, and the value is approximately equal to $1/(\omega\cdot\varepsilon_\mathrm{f})$, which can be used in subsequent studies to determine the formation dielectric constant (Fig. 4(d)). Interestingly, it was also found that at low frequency, the strength of the imaginary part of the current signal is weak, which causes problems such as difficulty in measurement, and it is necessary to choose a relatively high transmitting frequency for detection (Habashy et al., 2017; Guner et al., 2021).

For a radial two-layer formation model with a mud standoff of 1.0 mm, the resistivity of the mud and the relative permittivity are 8000 $\Omega\cdot$m and 6 respectively. When the working frequencies are 2, 5, and 10 MHz, the apparent resistivity curves obtained by calibration based on the numerical simulation results are shown in Fig. 5(a). Fig. 5(b) presents the calculated results of the apparent resistivity on a single electrode of the Halliburton's high-resolution oil-based mud imager (HROBMI) instrument under the same model, where f_1, f_2, and f_3 are three working frequencies increasing successively at the megahertz level (Guner et al., 2021). Due to the relatively small electrode size of the HROBMI instrument and the unknown working frequency, there are numerical differences in the calculated results of the apparent resistivity. However, the apparent resistivity curves in Fig. 5(a) and (b) exhibit good consistency in terms of their morphological characteristics, which can demonstrate that the numerical simulation method in this paper has relatively good applicability under this formation model.

Meanwhile, for the formation model with a mud standoff shown in Fig. 2, it can be seen from Eq. (4) that $\omega\cdot\varepsilon_\mathrm{m}$ and $\omega\cdot\varepsilon_\mathrm{f}$ tend to 0 at low frequency, and the loop impedance mainly depends on the conductivity of the mud and formation, and is less affected by the dielectric constant of the mud and formation. When the contrast between the mud and formation resistivity is large, the current may not be able to pass through the mud standoff into the formation, or the formation resistivity may contribute less to the measurement signal, resulting in problems such as shallow detection depth and poor detection performance of the instrument. It is then particularly important to select a suitable transmitting frequency. In addition, the setting of the electrode system will also affect the DOI of the instrument, and the influence of the instrument size on the resolution should be considered. Therefore, the optimization of transmitting frequency and electrode system parameters are the main content of the next section.

3. Optimization and selection of parameters

3.1. Selection of operating frequency

From the previous analysis and research, it is known that the transmitting frequency is the key factor that affects the signal magnitude and determines whether the current can flow into the formation. Therefore, we have investigated the signal response of the instrument in the presence of a mud standoff, with the numerical simulation results shown in Fig. 6.

Compared to Fig. 4, there are significant differences in the shape of the curves, particularly in the low frequency and low resistivity region. The real part of the current and impedance curves are separated, showing a non-linear relationship with the resistivity. And the signal is less sensitive to R_f, the lower the frequency, the narrower the sensitivity range (Fig. 6(a)–(c)). According to Fig. 6(a)–(c), for high frequency, such as 15 MHz and 20 MHz, the sensitivity range of current and impedance signals to the low resistance region increases, while the sensitivity to the high resistance region is not improved. For the real part of the current and the imaginary part of the impedance, the lower operating frequency can be more sensitive to the high-resistance formation. It can be seen from Fig. 6(d) that in the low frequency and low resistivity region, $|\Im((Z)/\Re(Z)|$ is a constant value, independent of R_f, approximately equal to $\omega\cdot\varepsilon_\mathrm{m}\cdot R_\mathrm{m}$, and only shows the property of the mud standoff. In this case, it can be assumed that the contribution of the measured signal comes mainly from the mud standoff, and the current has not (or less) flowed into the formation being measured and back to the return electrodes. In the mid and high frequency range, $|\Im((Z)/\Re(Z)|$ is numerically linearly related to R_f for different resistivity intervals. Therefore, the apparent resistivity and permittivity of the formation can be extracted by making plots or fitting equations under different calculation parameters.

Based on the analysis of the previous section, to ensure the effective measurement of the current signal, and according to the

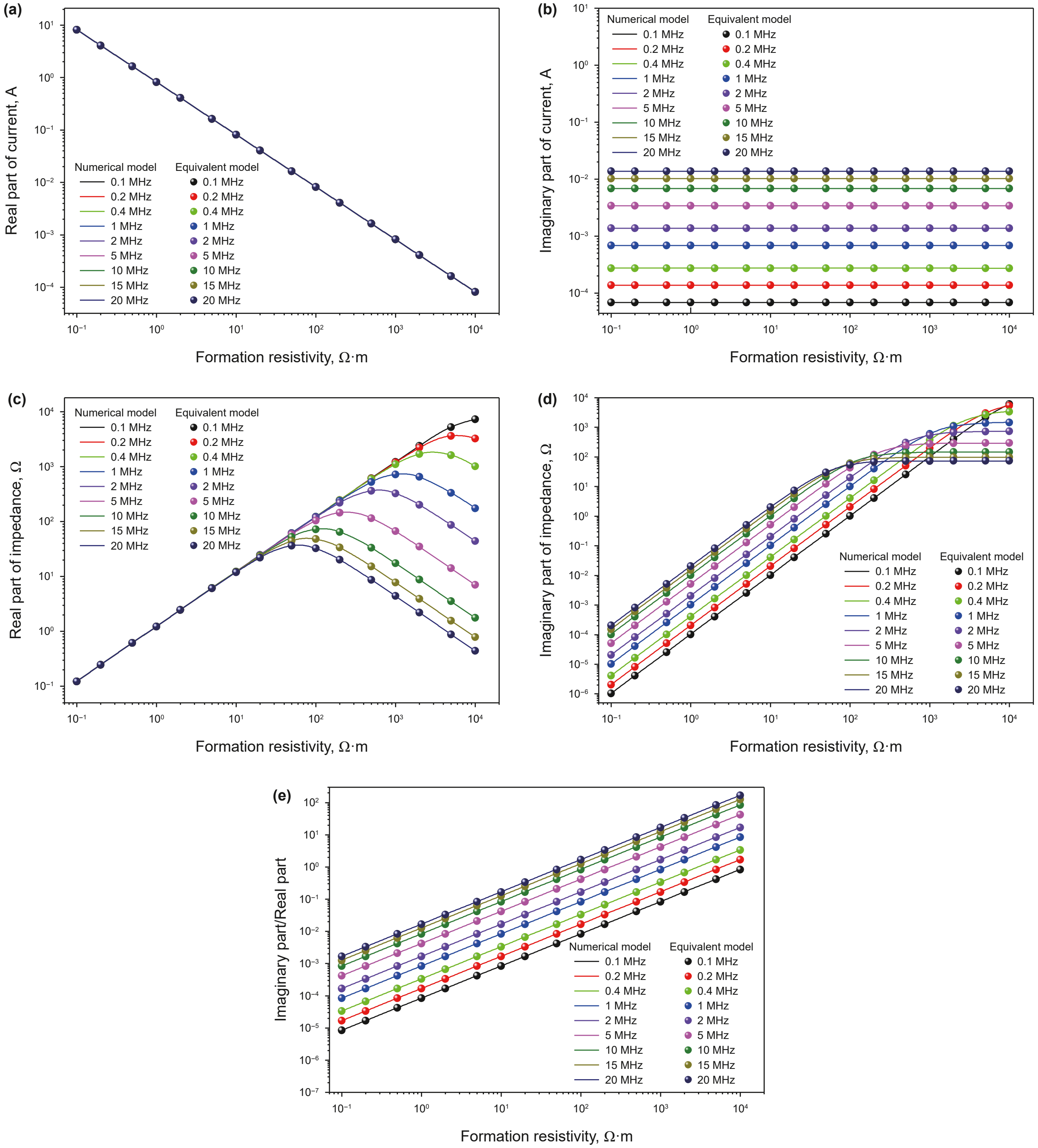

Fig. 4. Numerical simulation and equivalent circuit model calculation results of homogeneous formation: **(a)** real part of current; **(b)** imaginary part of current; **(c)** real part of impedance; **(d)** imaginary part of impedance; **(e)** ratio of imaginary part to real part of current (impedance).

sensitivity of the impedance signal to the formation resistivity in Fig. 6(a)–(c), 2, 5, and 10 MHz are selected as the transmitting frequencies of the instrument for further research.

3.2. Selection of electrode size

3.2.1. Electrode spacing

For the two formation models, the homogeneous formation and the formation with a mud standoff, the influence of the electrode spacing *L* on the current and impedance measurements is investigated. Except for the difference in numerical values, the response under the two formation models are consistent. Due to space limitations, only the calculation results of the formation model containing a mud standoff thickness of 0.1 mm are given, as shown in Fig. 7.

Fig. 7(a), (b) show that both the real and imaginary parts of current decrease as *L* increases in the high resistivity formation. When L increases to 15 cm, the current does not change significantly. The real part of the current curve coincides with the same R_f, while the imaginary part of the current curve coincides with the

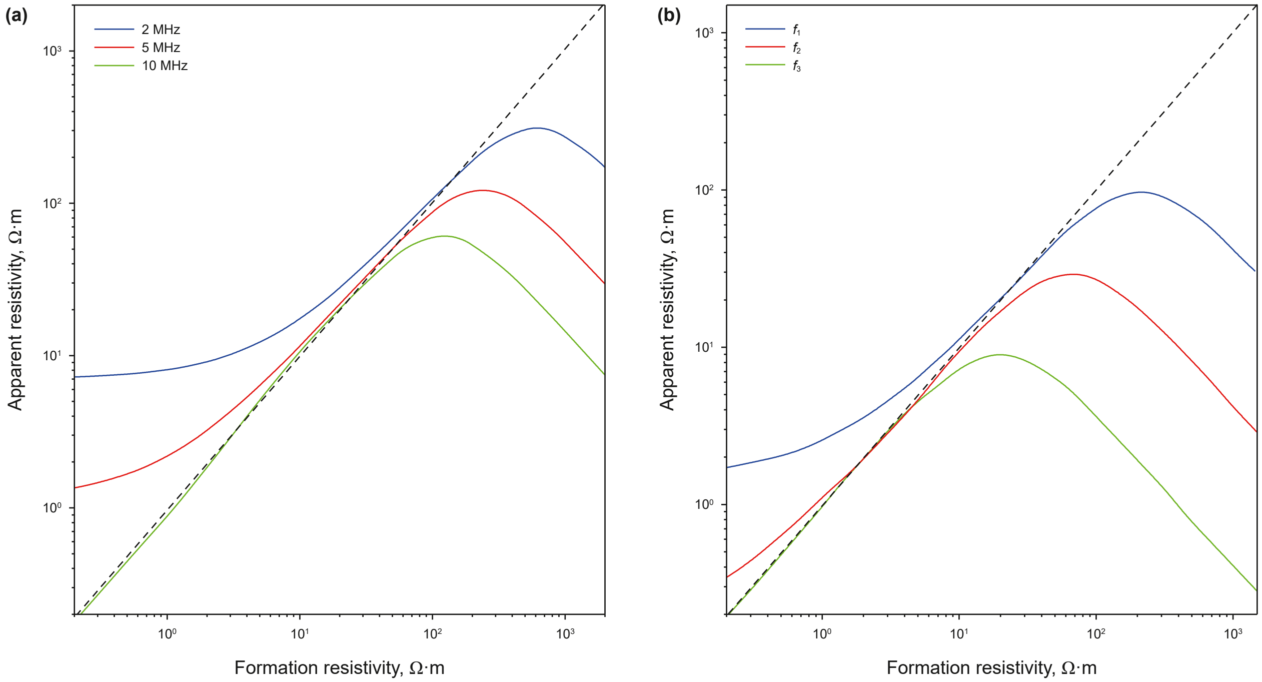

Fig. 5. Numerical simulation results of formation model with mud standoff and HROBMI instrument calculation results: **(a)** numerical simulation of the apparent resistivity response; **(b)** apparent resistivity response of HROBMI instrument.

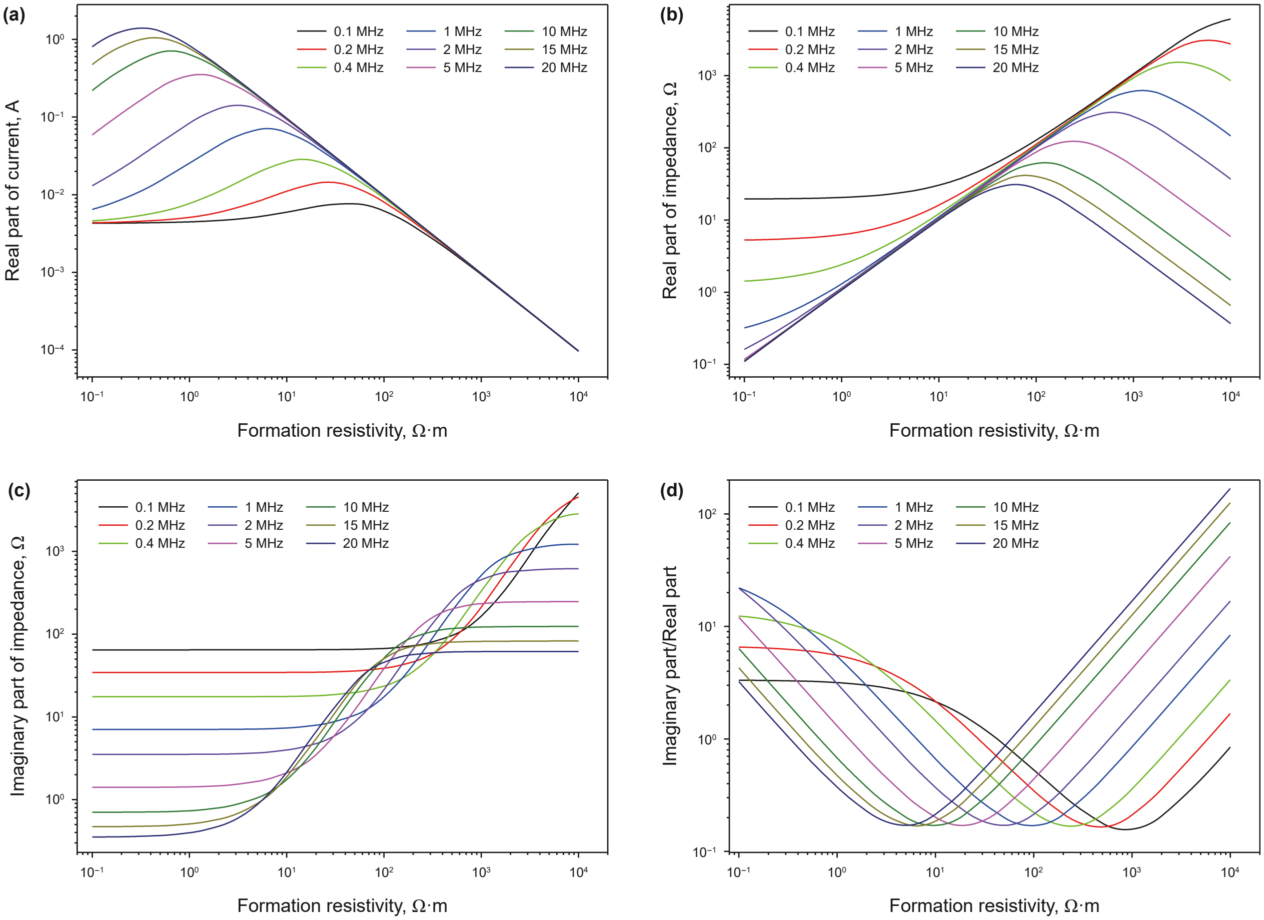

Fig. 6. Signal response at transmitting electrode in presence of mud standoff: **(a)** real part of current; **(b)** real part of impedance; **(c)** imaginary part of impedance; **(d)** ratio of imaginary part to real part of current (impedance). The thickness of the mud standoff is 0.1 mm, the resistivity and relative permittivity of the mud standoff are 10^5 Ω•m and 6, respectively.

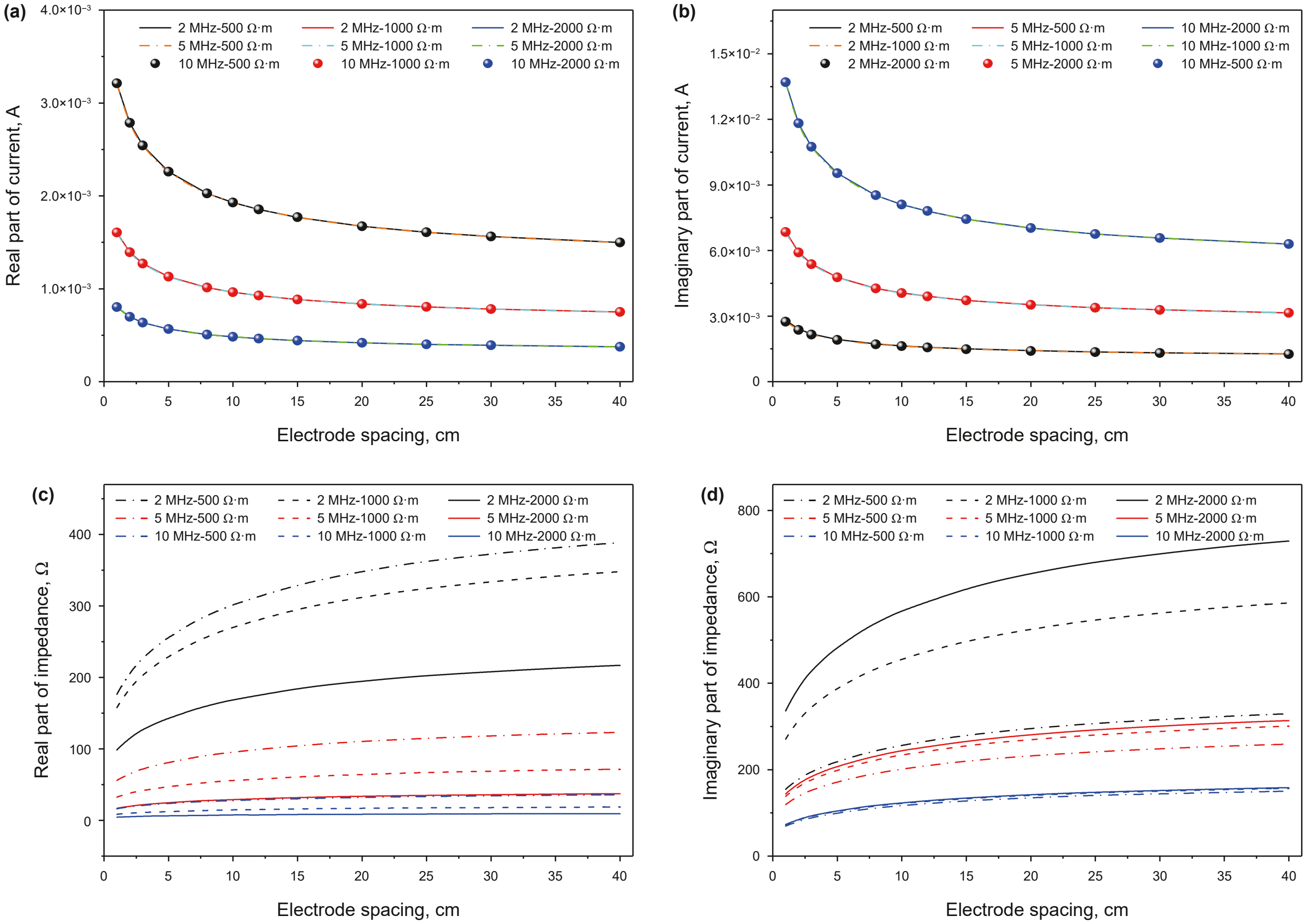

Fig. 7. Effect of electrode spacing on current and impedance measurements: **(a)** real part of current; **(b)** imaginary part of current; **(c)** real part of impedance; **(d)** imaginary part of impedance. The operating frequencies are 2, 5 and 10 MHz, R_f are 500, 1000 and 2000 Ω•m, respectively, the length of A0/A1/A1′ are 10 cm, L varies in the range [1,40] cm, the resistivity and relative permittivity of the mud standoff are 10^5 Ω•m and 6, respectively.

same transmitting frequency. Observing Fig. 7(c), (d) reveal that the real and imaginary parts of the impedance increase continuously as L increases, and the effect is more pronounced at lower formation resistivities. Similarly, as L continues to increase, the impedance measurement slows down and is less affected by L. Considering Eq. (6), when the parameters of the layer and the instrument are determined, the magnitude of the impedance depends on the depth (H_2) of the current flowing into the formation. In other words, by increasing the electrode spacing L, the current can flow deeper into the formation.

The above results show that the signal response of different formation resistivities is different when the electrode spacing L is changed. Therefore, we investigate the sensitivity of different L to the change in formation resistivity using the real part of the signal as an example. The transmitting frequency is 5 MHz, and L are 1, 5, 10, 20, and 40 cm, respectively. The $so = 0$ mm means that the standoff thickness is 0, that is, a homogeneous formation model. The changes in the current and impedance signals are shown in Fig. 8. The results show that the sensitivity of the real part of the current and impedance to the formation resistivity is consistent except for the difference in numerical value when the electrode spacing L is different, and is almost unaffected by L. In the high resistivity region, the real part of the current in the model with a standoff is slightly larger than that in the homogeneous formation, while the real part of the impedance shows the opposite result. In view of the analysis in the previous section, in the following study we take the electrode spacing L to be 7.5 cm.

3.2.2. *Electrode length*

To select the appropriate electrode size, the effect of the size of the transmitting and return electrodes on the signal response of the instrument was investigated in Figs. 9 and 10, respectively. The length of electrodes A0 and A1(A1′) varies from 1 to 25 cm. With the increase of A0 length, the real part of the current increases continuously. Notably, there is a significant increase in current in the range of 0–5 cm. Beyond this range, the increase in electrode length has a diminishing effect on the current, and the current increases more slowly as the formation resistivity increases (Fig. 9(a)). Conversely, the real part of the impedance decreases as the electrode length increases. Similarly, the real part of the impedance is significantly affected in the range of 0–5 cm and beyond this range the trend of change gradually slows down (Fig. 9(b)). The influence of the increase in the length of the return electrode A1 on the instrument's response is analogous to that of the transmitting electrode. Within the range of 0–10 cm, the real part of the current and impedance are significantly affected, and the effect gradually weakens thereafter (Fig. 10(a) and (b)).

The increase in the lengths of the transmitting electrode and the return electrode leads to an increase in the cross-sectional area through which the current flows in the equivalent circuit, resulting

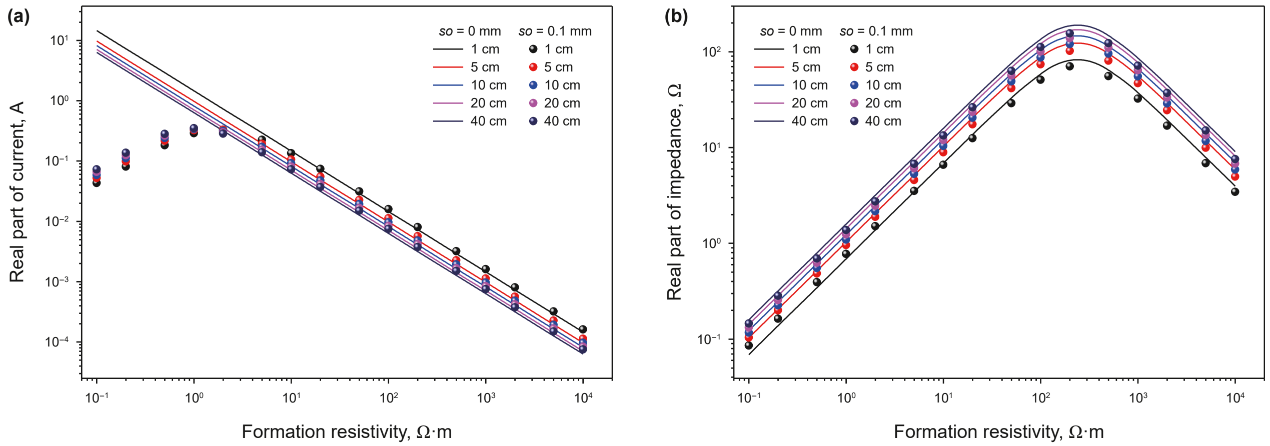

Fig. 8. Sensitivity of electrode spacing to formation resistivity: **(a)** real part of current; **(b)** real part of impedance.

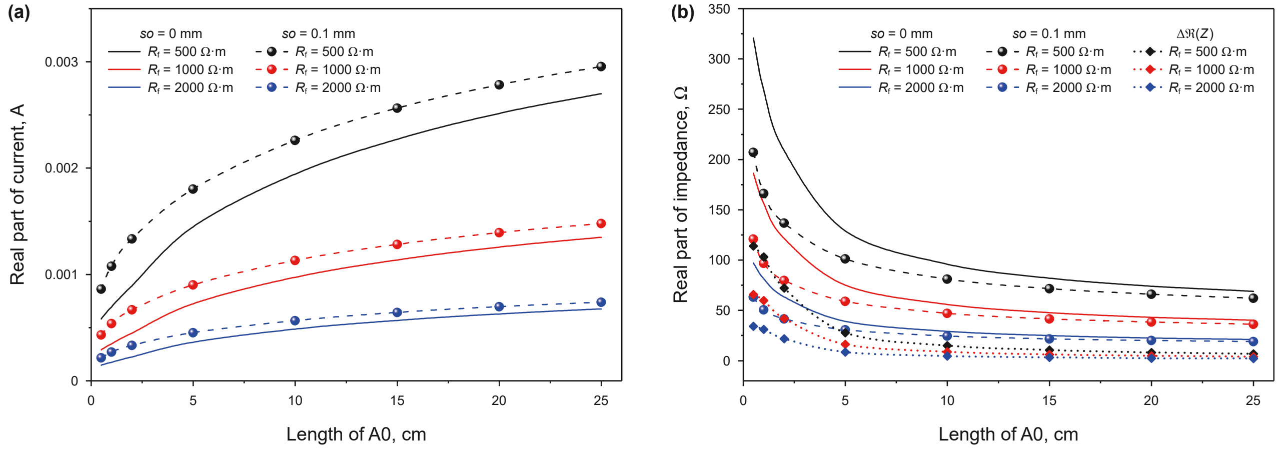

Fig. 9. Response of the instrument to changes in the length of the transmitting electrode: **(a)** Real part of current; **(b)** Real part of impedance. The resistivity and permittivity of the mud standoff are 10^5 Ω•m and 6, respectively.

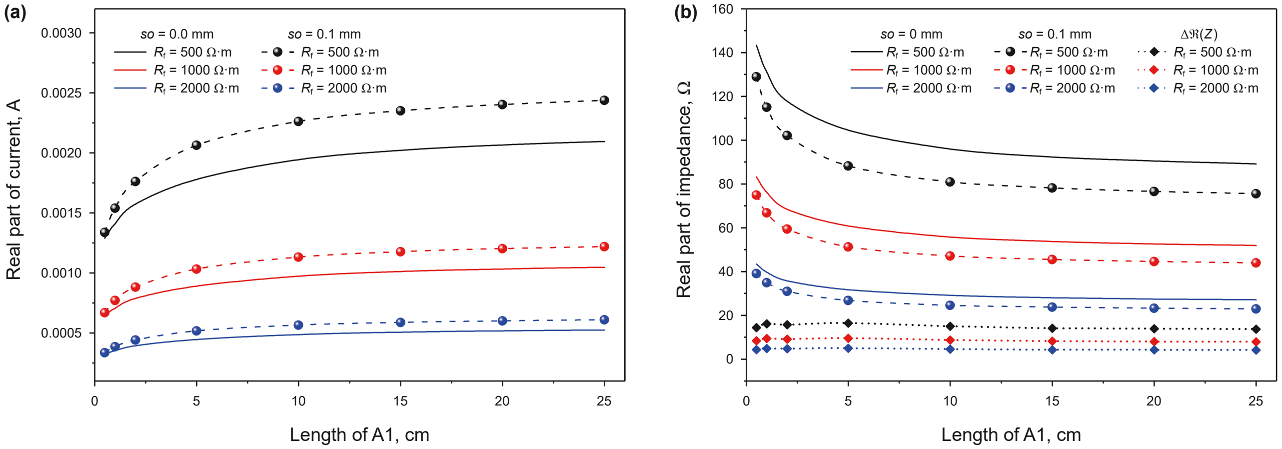

Fig. 10. Response of the instrument to changes in the length of the return electrode: **(a)** real part of current; **(b)** real part of impedance.

in a reduction of the equivalent resistance. This is manifested as the increase of current and the decrease of impedance in Figs. 9 and 10, which are consistent with the derivation results of Eq. (5). Additionally, as illustrated in Eq. (9) and Fig. 9(b), an increase in the length of A0 results in a continuous decrease in $\Delta\Re(Z)$, which approaches 0. This suggests that ΔH increases with the expansion of A0, although the incremental change becomes smaller. Similarly, Eq. (9) and Fig. 10 (b) indicate that as the length of A1 increases, $\Delta\Re(Z)$ continuously decreases and tends to remain constant, which suggests that ΔH continuously decreases with the increase of A1. In consideration of the impact of instrument dimensions on the DOI and the intensity of the measurement signal, the electrode dimensions of A0 = 5 cm and A1 = 10 cm have been selected for subsequent investigation.

3.3. Effect of mud standoff

3.3.1. Resistivity of mud standoff

The real part of the impedance curve diverges in the low resistivity region (<10 Ω•m) for different mud standoff resistivities at frequencies of 2 MHz and 5 MHz (Fig. 11(a)). The real part of the impedance is greater than that of the homogeneous formation model, as illustrated by the negative $\Delta\Re(Z)$ (which has been numerically inverted) in the red and blue dashed boxes in Fig. 11(b). At this juncture, the impedance of the mud dominates, given the substantial resistivity contrast and the predominant propagation of the current within the mud standoff. As the formation resistivity increases, i.e. the resistivity contrast decreases, the real part of the impedance curves for different mud resistivities overlap at the same frequency, as does $\Delta\Re(Z)$. At this point, the formation impedance dominates, and the measured impedance is less affected by the mud standoff resistivity. At a frequency of 10 MHz, the real part of the impedance curves of different mud standoff resistivities overlap across the entire range of measurements, indicating that high frequency can effectively realize the impedance shielding effect on mud standoff (Bespalov and Itskovich, 2008; Gao et al., 2017; Yang et al., 2021). This allows the current to penetrate the standoff and enter the formation to be measured even when the resistivity contrast is low.

3.3.2. Thickness of mud standoff

When the operating frequency is 5 MHz and the mud standoff thickness varies, the real part of the impedance curves shown in Fig. 12(a) also exhibit curve separation in the low resistivity region. The larger the *so* is, the greater the curve separation is. And $\Delta\Re(Z)$ is numerically larger (the negative value has been inverted, as in the red dashed box in Fig. 12(b)), where the impedance primarily reflects the property of the mud standoff. When the formation resistivity exceeds 10 Ω•m, the real part of the impedance curves for different *so* overlap, indicating that the impedance measurements are less affected by the thickness of the mud standoff. Consequently, in layers of high resistivity, the mud standoff impedance can be subtracted as a base value to obtain the formation apparent impedance and subsequently calculate the formation apparent resistivity.

3.4. Depth of investigation and vertical resolution

3.4.1. Depth of investigation

The depth of investigation is an important indicator to characterize the detection performance of logging instruments (Wu et al., 2022, 2023). It reflects the sensitivity of the instrument to changes in the radial properties of the formation. Referring to the definition of the geometric factor of induction logging, this paper defines the relative contribution of the cylindrical medium of radius r_t to the apparent impedance in a formation of infinite thickness as the pseudo-geometric factor (G_p) (Kang et al., 2018; Wu et al., 2022). We defined pseudo-geometric factors by using measured values of the real part of the impedance.

$$G_p = \frac{\Re(Z_a) - \Re(Z_t)}{\Re(Z_i) - \Re(Z_t)} \tag{11}$$

where $\Re(Z_a)$ represents the measured value of the real part of the impedance when the invasion depth changes, $\Re(Z_t)$ represents the measured value of the real part of the impedance when there is no invasion, and $\Re(Z_i)$ represents the measured value of the real part of the impedance when the invasion radius is infinite.

The invasion radius varies from 0 to infinity, and the pseudo-geometric factor is shown in Fig. 13. If the invasion radius is defined as the DOI of the instrument when G_p is 0.5, and the transmitting frequency is 2 MHz, the DOI is approximately 2.43 cm for different resistivity contrast ratios. If it is considered that G_p is equal to 0.9, the corresponding invasion radius is the DOI of the instrument and the DOI then increases to 8.74 cm (3.44 inch). In contrast, the nominal DOI of Schlumberger's OBMI instrument is 8.89 cm (3.5 inch), which is slightly greater than the detection depth under the current instrument design (Cheung et al., 2001; Sembiring et al., 2005; Zohrehet al., 2014; Lai et al., 2018). Meanwhile, under the two different resistivity contrasts, the detection depth of the instrument is greater than that at the frequencies of 5 MHz and 10 MHz when the operating frequency is 2 MHz, indicating that the detection depth of the instrument cannot be improved by constantly increasing the frequency.

3.4.2. Vertical resolution

A three-layer stratigraphic model, illustrated in Fig. 14(a), is employed to evaluate the vertical resolution of the instrument. The target formation thicknesses in the model are H = [0.02, 0.05, 0.1,

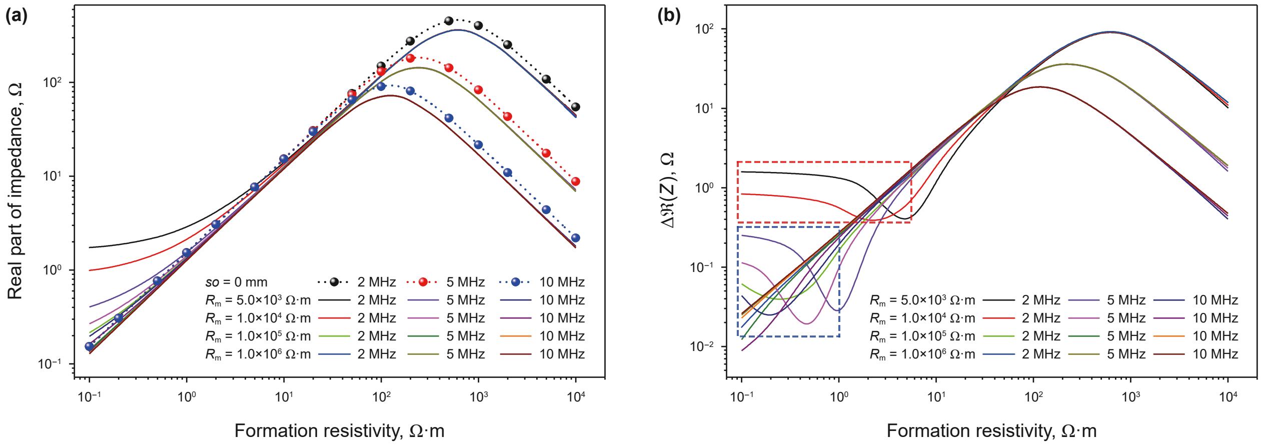

Fig. 11. Effect of mud standoff resistivity on instrument response: **(a)** real part of impedance; **(b)** $\Delta\Re(Z)$. The thickness of the mud standoff is 0.01 mm and the relative permittivity is 6.

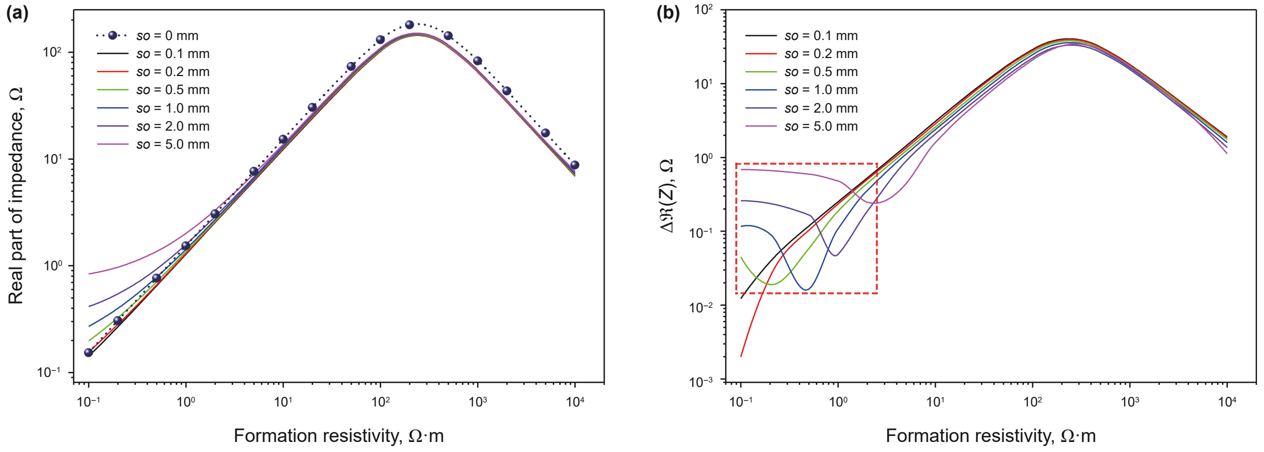

Fig. 12. Effect of mud standoff thickness on instrument response: **(a)** real part of impedance; **(b)** $\Delta\Re(Z)$. The operating frequency is 5 MHz, the resistivity and relative permittivity of the mud standoff are 10^5 Ω m and 6, respectively.

0.2, 0.4, 0.8, 1.0] m, with the surrounding rock assumed to be infinitely thick on both sides. Additionally, a mud standoff with a thickness of 0.01 mm is considered.

The results demonstrate that the apparent resistivity is in close approximation with the true resistivity, even for a target formation thickness of 2 cm, and can be effectively identified by the response of the instrument. However, similar to lateral logging, the influence of the wellbore mud and surrounding rock results in a corner effect in the curve (Tan et al., 2014; Kang et al., 2018). As shown in Fig. 14(b), when the layer thickness exceeds 5 cm (the length of A0), the horn effect disappears, and as the layer thickness continues to increase, the apparent resistivity aligns more closely with the true resistivity of the formation, which is less influenced by the surrounding rock (Hu et al., 2019).

The OBMI instrument also has an acceptable resistivity calculation error, depending on the resistivity contrast, with an effective resolution (vertical and horizontal) of 3.048 cm (1.2 inch). The minimum vertical resolution for oil-based mud imaging instruments from several other companies is as low as 0.508 cm (0.2 inch). In fact, for the detection in highly-resistive formations, we are more concerned with the DOI of the instrument, while the

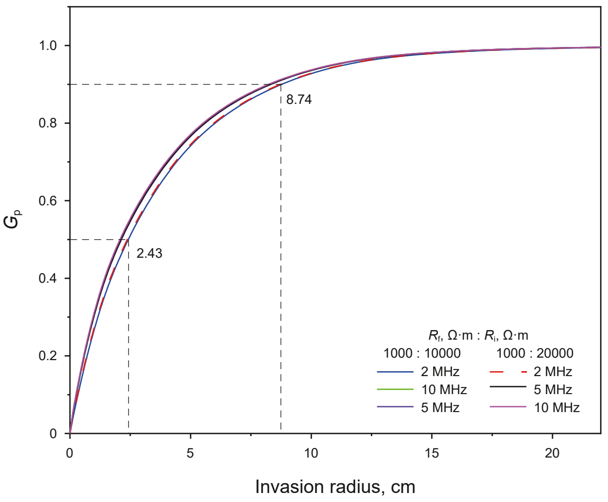

Fig. 13. Pseudo-geometric factor and depth of investigation. The relative permittivity of the invasion zone is 10, the thickness of the mud standoff is 0.01 mm, and the resistivity and relative permittivity of the mud standoff are 10^5 Ω•m and 6, respectively.

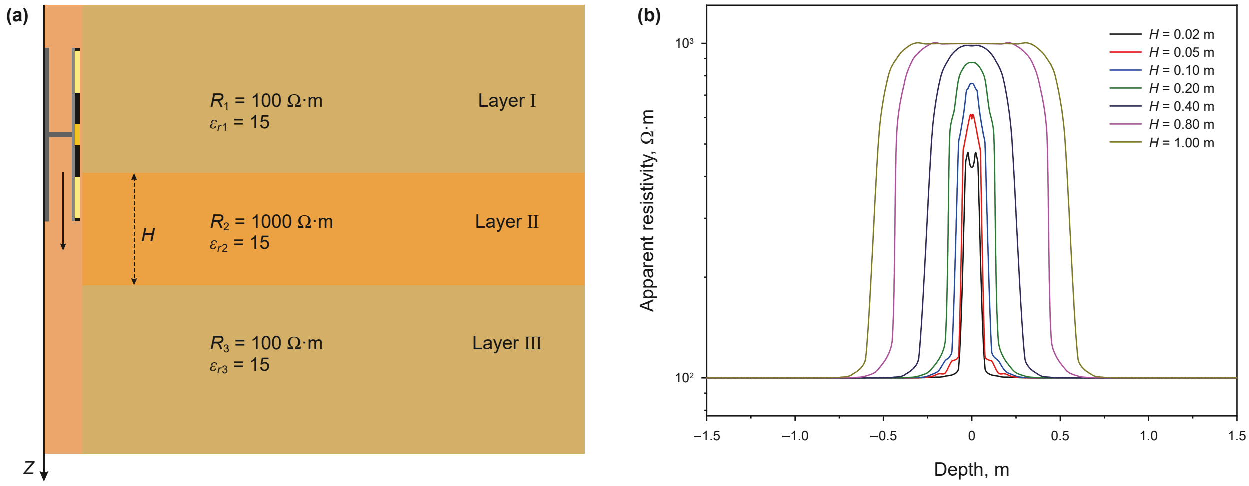

Fig. 14. Vertical resolution of the instrument: **(a)** three-layer formation model; **(b)** response of a three-layer formation model. The operating frequency is 2 MHz.

vertical resolution of the instrument is generally related to the size of the main electrode. Therefore, in the next section we will carry out a new instrument design based on the above study to achieve a further increase in the detection depth of the instrument.

4. Design of new instrument and detection capability

To mitigate the influence of the borehole and surrounding rock on formation resistivity measurements and enhance the DOI of the instrument, a new focusing instrument has been developed based on prior research, and its detection capability is evaluated.

4.1. Design of new focusing instrument

The structural parameters of the instrument and the current focusing method are shown in Fig. 15. The instrument is constructed by placing a pair of symmetrical focusing (bulking) electrodes B1 and B1′ on either side of the main electrode A0, leaving the return electrodes unchanged. A voltage of equal intensity (1 V) is applied to the main electrode A0 and the focusing electrode B1/B1′ to ensure that the potential between them is equal, so that no current flows between the electrodes (Evan and Burt, 2002). The two symmetrical return electrodes are earthed and the potential is kept at 0 V. To enhance the focusing effect, B1/B1′ are typically longer than A0. Due to the current focusing effect of the focusing electrodes, the current emitted by A0 flows perpendicularly into the formation in the form of a current beam, which in turn increases the DOI of the instrument.

4.2. Detection performance

The results of the pseudo-geometric factors calculation for the focused instrument and the unfocused instrument of the same size are shown in Fig. 16. In Fig. 16(a), the pseudo-geometric factor of the unfocused instrument with the dimensions of the transmitting electrode A0 $= 25$ cm, electrode spacing $L = 7.5$ cm and return electrode A1 $= 10$ cm is shown in the black curve. The DOIs of the two instruments with G_p equal to 0.5 are 3.96 cm and 5.82 cm, respectively. And the DOIs with G_p equal to 0.9 are 13.42 cm and 17.40 cm, respectively. Similarly, the DOI of the focused instrument at different frequencies and different resistivity contrasts is similar to that of the unfocused instrument in Section 3.4.1, with the maximum DOI at 2 MHz (Fig. 16(b)). The unfocussed instrument has the same dimensions as the focused instrument, and although its detection depth is greatly improved compared to the previous A0 $= 5$ cm, it also suffers a severe loss of vertical resolution (not shown). In contrast, the DOI of the focused instrument is almost twice that of the OBMI instrument, which is an effective improvement in detection depth, and its vertical resolution can still reach 2 cm, as shown in Fig. 17(a).

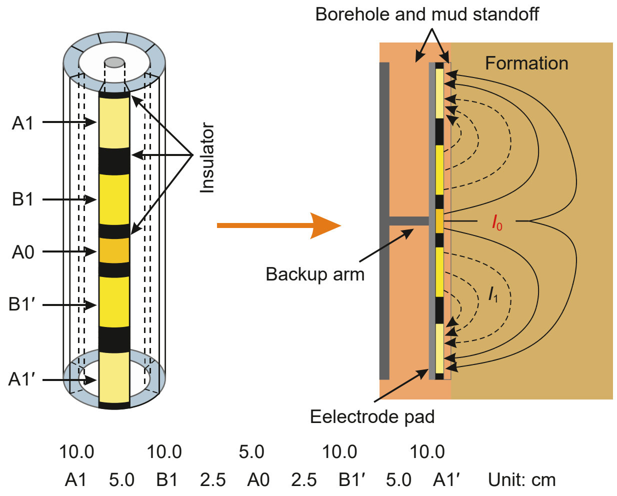

Fig. 15. Current focusing and design of new logging instrument in OBM.

For the three-layer formation model in Fig. 14, the response of the focusing instrument was calculated as shown in Fig. 17(a). The results show that the apparent resistivity curves of the focusing instruments have an obvious horn phenomenon near the layer interface, but it can still effectively identify the formation. The horn phenomenon may be caused by high frequency oscillation due to high transmitting frequency. Compared with the unfocused instrument, the focused instrument is more effective in identifying thin layers, and the calculation error between apparent resistivity and true resistivity is reduced.

The Oklahoma formation derives its name from the stratigraphic variations across lithologies with huge variations in formation resistivities. Consequently, the Oklahoma formation model is widely utilized as a standard for assessing the detection capabilities of electrical logging instruments (Deng et al., 2021). The model stratigraphic parameters are presented in Table 1 for reference. The stratigraphic sequence comprises a total of 19 layers. The surrounding rocks on both sides are infinitely thick strata, and the thickness of the middle stratum varies between 0.5 and 4.0 m. The formation resistivity varies within the range of 50–2000 Ω•m, which is consistent with the characteristics of the logging environment and the relative dielectric constants of the layers, which are all 15. The results of the calculations are presented in Fig. 17(b). The apparent resistivity curve can accurately represent the true resistivity and formation interface of thicker layers, and also has a good ability to identify thin layers. It is shown that the new focusing instrument developed in this paper has good formation resolution.

5. Conclusions and discussions

In this paper, a high-frequency focused electrode-type electrical logging method is proposed to achieve effective detection of high-resistance formations in OBM borehole environments. For OBM logging environments, a current path between the formation and the instrument is achieved by applying a high-frequency voltage source to the electrode-type instrument in the form of a displacement current. The megahertz operating frequency effectively shields the impedance of the mud standoff, making measurements of formation resistivity possible. The design of high-frequency focused electrode-type instrument enables effective identification of 2 cm thin layers, which is comparable to the vertical resolution of existing instruments in OBM. The DOI of the instrument has been improved with the existing design. Compared with the existing electrical imaging instrument in OBM, the detection depth is increased by nearly two times. At operating frequency of 2 MHz, the detection depth can reach 17.40 cm. and the focusing instruments perform well in complex models with continuous changes in stratigraphic properties.

The findings of this study can serve as a point of reference and provide guidance for the detection of the resistivity in highly-resistive formations drilling with OBM and the design of electrical logging instrument, and we will carry out more physical experiments and work on instrument manufacturing. However, there are still some issues that require further investigation and resolution. For instance, an alternative approach would be to select a more refined operating frequency, thereby attenuating the oscillatory characteristics associated with high frequencies. Another potential solution would be to leave the focusing electrode unloaded or to

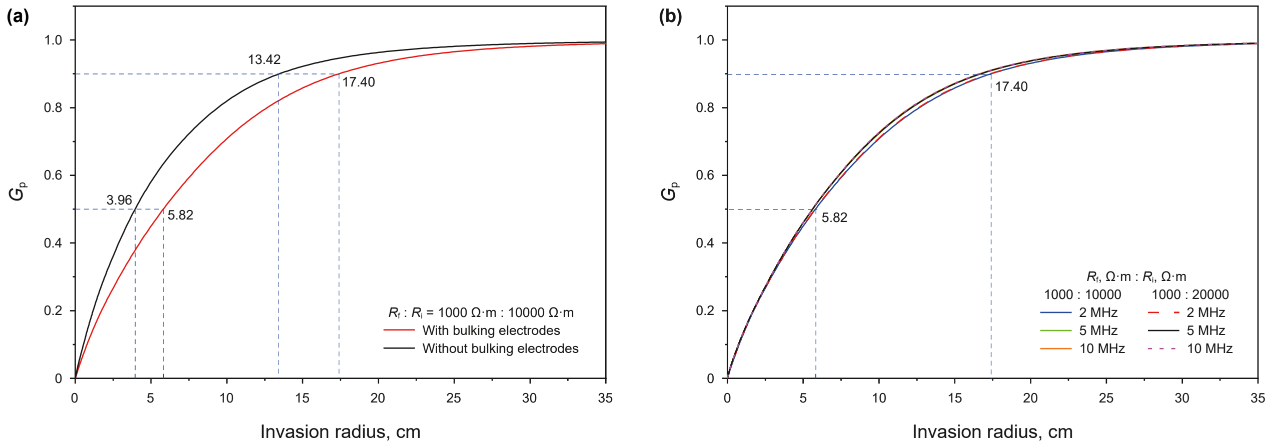

Fig. 16. Invasion radius and pseudo-geometric factor: **(a)** comparison of DOI between focused instrument and unfocused instrument; **(b)** pseudo-geometric factor and detection depth of focused instrument.

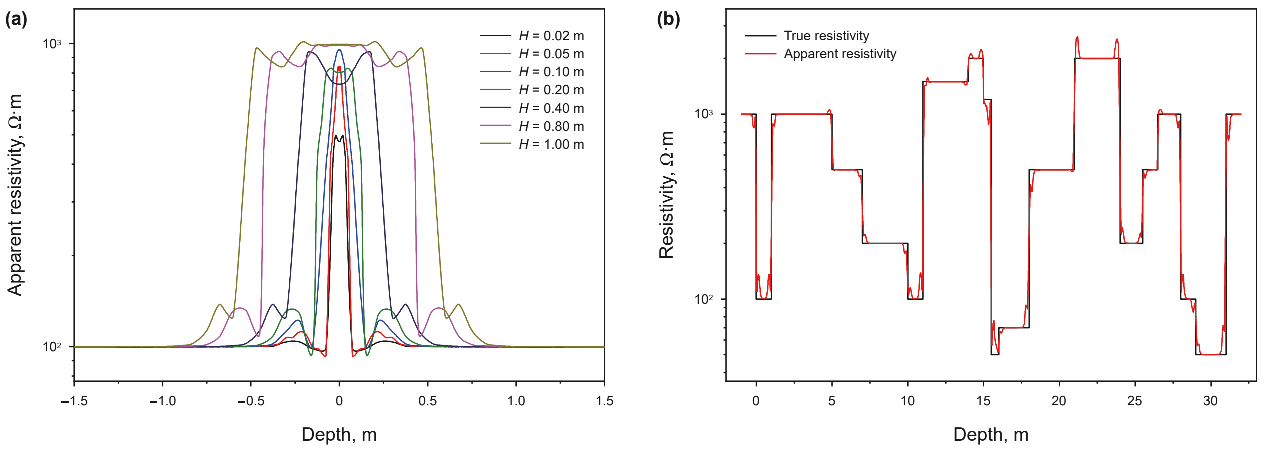

Fig. 17. Response of the three-layer formation model **(a)** and Oklahoma formation model **(b).**

Table 1
Parameters of Oklahoma formation model.

Layer	R_f, Ω·m	Thickness, m	Layer	R_f, Ω·m	Thickness, m
1	1000	–	11	70	2.0
2	100	1.0	12	500	3.0
3	1000	4.0	13	2000	3.0
4	500	2.0	14	200	1.5
5	200	3.0	15	500	1.0
6	100	1.0	16	1000	1.5
7	1500	3.0	17	100	1.0
8	2000	1.0	18	50	2.0
9	1200	0.5	19	1000	–
10	50	0.5	–	–	–

apply a reduced focusing voltage, which would result in two shallower detection depth, thus addressing the varying probing requirements. Furthermore, a significant area for future investigation is the effective correction of the mud standoff effect and the extraction of dielectric constant information. Quantitative inversion of the parameters involved in the numerical simulation will also be an interesting work.

CRediT authorship contribution statement

Kang-Kang Wu: Writing – original draft, Validation, Software, Investigation, Formal analysis. **Lei Wang:** Methodology, Funding acquisition, Conceptualization. **Shao-Gui Deng:** Supervision, Project administration, Funding acquisition. **Xue-Wen Kou:** Writing – review & editing, Investigation, Data curation.

Declaration of competing interest

The authors declare that they have no known competing financial interests or personal relationships that could have appeared to influence the work reported in this paper.

Acknowledgements

The authors would like to acknowledge the support of the National Natural Science Foundation of China (42074134, 42474152, 42374150), CNPC Innovation Found (2024DQ02-0152).

References

Aguilera, R.F., Radetzki, M., 2014. The shale revolution: global gas and oil markets under transformation. Miner. Econ. 26, 75–84. https://doi.org/10.1007/s13563-013-0042-4.

Bespalov, A.N., Itskovich, G.B., 2008. High resolution resistivity earth imager. U.S. patent 7 (397), 250.

Bloemenkamp, R., Zhang, T., Comparon, L., et al., 2014. Design and field testing of a new high-definition microresistivity imaging tool engineered for oil-based mud. In: SPWLA 55th Annual Logging Symposium. Abu Dhabi, United Arab

Emirates.

Chen, M.Y., 2001. Methods and apparatus for imaging earth formation with a current source, a current drain, and a matrix of voltage electrodes therebetween. U.S. Patent 6 (191), 588.

Cheung, R., Pittman, D., Hayman, A., et al., 2001. Field test results of a new oil-base mud formation imager tool. In: SPWLA 42nd Annual Logging Symposium. Houston, Texas.

Christie, R., Schoch, P., 2007. Structural and sedimentary features delineated using electrical borehole images in a non-conductive mud system. In: SPWLA 48th Annual Logging Symposium. Austin, Texas.

Davis, L.A., 2018. The shale oil and gas revolution. Engineering 4 (4), 438–439. https://doi.org/10.1016/j.eng.2018.06.003.

Deng, S.G., Liu, T.L., Cai, L.Y., et al., 2021. Fast extraction of horizontal formation resistivity based on multi-component induction logging and its application. Chin. J. Geophys. 64 (6), 2199–2209. https://doi.org/10.6038/cjg2021O0265 (in Chinese).

Evan, M.T., Burt, A.R., 2002. Image focusing method and apparatus for wellbore resistivity imaging. U.S. Patent 6, 348–796.

Færgestad, I.M., Strachan, C.R., 2014. Developing a high-performance oil-base fluid for exploration drilling. Oilfield Rev. 26 (1), 26–33.

Gao, J.S., Sun, J.M., Jiang, Y.J., et al., 2017. Weighted processing for microresistivity imaging logging in oil-based mud using a support vector regression model. Geophysics 82 (6), D341–D351. https://doi.org/10.1190/geo2016-0592.1.

Gao, J.S., Jiang, L.M., Liu, Y.P., et al., 2019. Review and analysis on the development and applications of electrical imaging logging in oil-based mud. J. Appl. Geophys. 171, 103872. https://doi.org/10.1016/j.jappgeo.2019.103872.

Gao, J., Ma, Y.N., Jiang, L., et al., 2024. Research on quantitative inversion characterization of high-definition electrical imaging logging in oil-based mud based on backpropagation neural network and multiple population genetic algorithm-Levenberg-Marquardt algorithm. Geophysics 89 (3), D171–D181. https://doi.org/10.1190/geo2023-0468.1.

Growcock, F.B., Ellis, C.F., Schmidt, D.D., 1994. Electrical stability, emulsion stability, and wettability of inverted oil-based muds. SPE Drill. & Compl. 9 (1), 39–46. https://doi.org/10.2118/20435-PA.

Guner, B., Fouda, A.E., Ewe, W.B., et al., 2021. Quantitative demonstration of a high-fidelity oil-based mud resistivity imager using a controlled experiment. Petrophysics 62 (4), 407–421. https://doi.org/10.30632/PJV62N4-2021a5.

Habashy, T., Hayman, A., Chen, Y.H., et al., 2017. System and method for imaging properties of subterranean formations. U.S. Patent 9 (678), 239.

Hindry, H.W., 1941. Characteristics and application of an oil-base mud. OR Trans. 142 (1), 70–75. https://doi.org/10.2118/941070-G.

Hong, D.C., Yang, S.D., 2011. Multi-component induction logging response in large dielectric formation. Acta Phys. Sin. 60 (10), 109101. https://doi.org/10.7498/aps.60.109101 (in Chinese).

Hou, J.S., Sanmartin, L., Wu, D.G., et al., 2013. Real-time borehole correction of multicomponent induction data acquired in OBM wells: algorithm and applications1. Petrophysics 54 (2), 128–141.

Hu, S., Chen, L., Wang, J., 2019. Fast inversion of array laterolog measurements in an axisymmetric medium. Appl. Geophys. 16, 539–548. https://doi.org/10.1007/s11770-019-0767-0.

Jiang, Z.H., Fu, J.H., Li, G.R., et al., 2021. Using resistivity data to study the waterflooding process: a case study in tight sandstone reservoirs of the Ordos Basin, China. Geophysics 86 (2), B55–B65. https://doi.org/10.1190/geo2020-0401.1.

Kang, Z.M., Ke, S.Z., Li, X., et al., 2018. 3D FEM simulation of responses of LWD multimode resistivity imaging sonde. Appl. Geophys. 15, 401–412. https://doi.org/10.1007/s11770-018-0692-7.

Ke, S.Z., 2008. Full 3-D numerical modeling of borehole electric image logging and the evaluation model of fracture. Sci. China, Ser. A D. 51 (2), 170–173. https://doi.org/10.1007/s11430-008-6021-x.

Lai, J., Wang, G.W., Wang, S., et al., 2018. A review on the applications of image logs in structural analysis and sedimentary characterization. Mar. Petrol. Geol. 95, 139–166. https://doi.org/10.1016/j.marpetgeo.2018.04.020.

Li, C.L., Li, C.X., Hou, Y.T., et al., 2015. Well logging evaluation of triassic chang 7 member tight reservoirs, yanchang formation, ordos basin, NW China. Petrol. Explor. Dev+. 42 (5), 667–673. https://doi.org/10.1016/S1876-3804(15)30061-6.

Morton, K., Bomar, B., Schiller, M., et al., 2005. Selection and evaluation criteria for high-performance drilling fluids. In: SPE Annual Technical Conference and Exhibition. Dallas, Texas. https://doi.org/10.2118/96342-MS.

San, M.L., Kainer, G., Elliott, J.P., et al., 2008. Oil-based mud imaging tool generates high quality borehole images in challenging formation and borehole condition, including thin beds, low resistive formations, and shales. In: SPWLA 49th Annual Logging Symposium. Austin, Texas.

Sembiring, P., Agustinus, S.R., Bashir, N., et al., 2005. Oil-based mud micro-imager (OBMI) application in Sangatta: a field case study. In: SPE Asia Pacific Oil and Gas Conference and Exhibition. Jakarta, Indonesia. https://doi.org/10.2118/92779-MS.

Tan, M.J., Wang, P., Li, J., et al., 2014. Numerical simulation and fracture evaluation method of dual laterolog in organic shale. J. Appl. Geophys. 100, 1–13. https://doi.org/10.1016/j.jappgeo.2013.10.006.

Thaemlitz, C.J., 2004. Electrically conductive oil-based mud. U.S. Patent 6, 691–805.

Wang, B., Liu, X.j., Sima, L.Q., 2019. Grading evaluation and prediction of fracture-cavity reservoirs in Cambrian Longwangmiao formation of Moxi area, Sichuan Basin, SW China. Petrol. Explor. Dev+. 46 (2), 290–301. https://doi.org/10.1016/S1876-3804(19)60010-8.

Wang, L., Fan, Y.R., Gao, Y.W., et al., 2017. Numerical simulation and characteristics analysis of dual laterolog in cavernous reservoirs on the basis of 3D-FEM. Chin. J. Geophys. 60 (5), 2011–2019. https://doi.org/10.6038/cjg20170532 (in Chinese).

Wu, Y.Z., Wu, Z.G., Fan, Y.R., et al., 2022. Numerical and physical simulations of array laterolog in deviated anisotropic formation. Pet. Sci. 19 (5), 2107–2119. https://doi.org/10.1016/j.petsci.2022.03.023.

Wu, Y.Z., Fan, Y.R., Cai, L.Y., et al., 2023. Detection performance and grading-selection-based inversion of low-frequency alternating current resistivity logging in moderate-high resistance formations. SPE J. 28 (1), 355–370. https://doi.org/10.2118/212273-PA.

Yang, S., Brill, T.M., Abellan, A., et al., 2021. Carbonate reservoir characterization with high-resolution logging-while-drilling dual-images in oil-based mud. In: Abu Dhabi International Petroleum Exhibition and Conference. Abu Dhabi, UAE. https://doi.org/10.2118/207219-MS.

Zanten, R.V., 2014. Electrically conductive oil-based drilling fluids. U.S. Patent 8 (763), 695.

Zohreh, M., Radzuan, J., Zeynalabedin, S., et al., 2014. Formation evaluation in dezful embayment of Iran using oil-based-mud imaging techniques. J. Petrol. Sci. Eng. 121, 23–37. https://doi.org/10.1016/j.petrol.2014.05.019.

Zou, C.N., Pan, S.Q., Jing, Z.H., et al., 2020. Shale oil and gas revolution and its impact. Acta Pet. Sin. 41 (1), 1–12. https://doi.org/10.7623/syxb202001001 (in Chinese).